

UKAEA-CCFE-PR(18)7

T D Swinburne and S L Dudarev

Kink-limited Orowan strengthening explains the ductile to brittle transition of irradiated and unirradiated bcc metals

Enquiries about copyright and reproduction should in the first instance be addressed to the UKAEA Publications Officer, Culham Science Centre, Building K1/0/83 Abingdon, Oxfordshire, OX14 3DB, UK. The United Kingdom Atomic Energy Authority is the copyright holder.

Kink-limited Orowan strengthening explains the ductile to brittle transition of irradiated and unirradiated bcc metals

T D Swinburne¹ and S L Dudarev²

¹Theoretical Division T-1, Los Alamos National Laboratory, Los Alamos, NM, 87545, USA

²CCFE, Culham Science Centre, Abingdon, Oxon, OX14 3DB, UK

Kink-limited Orowan strength explains the ductile to brittle transition of irradiated and unirradiated bcc metals

T D Swinburne

Theoretical Division T-1, Los Alamos National Laboratory, Los Alamos, NM, 87545, USA

S L Dudarev

CCFE, Culham Science Centre, Abingdon, Oxon, OX14 3DB, UK

(Dated: May 1, 2018)

The line tension model of obstacle hardening is modified to account for the thermally activated, kink-limited glide of $1/2\langle 111 \rangle$ screw dislocations, allowing application to the plastic flow of bcc metals. Using atomistically-informed dislocation mobility laws, Frenkel-Kontorova simulations and a simplified dislocation obstacle model, we identify a new size effect for intermediate obstacle densities, where the activation energy for screw dislocation motion halves once the obstacle density falls below a critical value. Our model shows striking agreement with fracture experiments across a wide range of unirradiated and irradiated bcc metals. In particular, we demonstrate that the presence of defects in the crystal lattice can at most double the ductile to brittle transition temperature.

The motion of a dislocation line through a random field of static obstacles is a classic problem of theoretical metallurgy^{1–7}. Whilst obstructions to dislocation motion in real materials are diverse, including forest dislocations, point defect clusters, solute atoms, precipitates, voids and gas bubbles amongst others⁸, many models do not focus on specifics of the dislocation-obstacle interaction mechanism^{9–12}, instead assigning a threshold obstacle bypass stress then gauging the effect of the obstacle distribution on the flow stress⁴. The model is further simplified by treating the elastic self energy of the dislocation, which is in principle given by a sum of an orientation-dependent line energy and its second derivative¹³, by an isotropic line tension $\mu b^2/2$, where μ is the shear modulus and b is the Burgers vector of the dislocation¹. The resultant model has a powerful generality which has been widely studied in materials science and statistical physics^{14,15}.

The prototypical configuration of such models is shown in the left of figure 1. An applied shear stress σ exerts a total force $b\sigma L$ on a dislocation pinned between two obstacles spaced by L , resulting in the dislocation forming a circular arc with a radius of curvature $\mu b/2\sigma$. Obstacle bypass occurs once the total force on the obstacle pinning the dislocation line exceeds some defined threshold f_{th} , allowing the dislocation to shear through the obstacle, or the total force causes the radius of curvature for two neighboring segments to fall below $L/2$, whereupon the segments combine and 'pinch off'^{1,8}. The threshold condition $f_{th} = b\sigma_F L$ thus yields $\sigma_F = f_{th}/(bL)$ for a single segment. Applying this relation to an obstacle distribution, theoretical hardening laws and line tension simulations all exhibit the famous Friedel relationship^{3–7} $\sigma_F = \alpha\mu b/\langle L \rangle$, where $\langle L \rangle$ is the average obstacle spacing and α is a dimensionless constant dependent on the obstacle distribution.

Models of obstacle hardening are of clear relevance to irradiation induced embrittlement, where a relatively clean initial microstructure is populated with an increasing

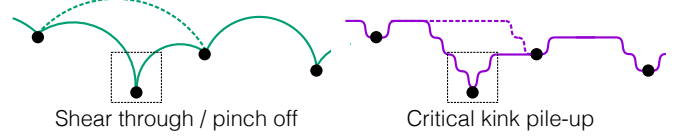


FIG. 1. Left: a simple elastic dislocation line pinned to obstacles under an applied stress. Obstacle bypass occurs once the applied stress exceeds a certain threshold value inversely proportional to the distance between obstacles. Right: the same model with a kink-mediated dislocation mobility mechanism. Obstacle bypass occurs once the stress on the kink pile-up exceeds a threshold that is independent of the obstacle separation, provided that the two pile-ups do not meet (see figure 2).

density of nanoscale defects under irradiation, which impede dislocation motion⁸. The ability to predict the conditions under which irradiation induced embrittlement occurs remains a critical objective for nuclear materials science¹⁶, in particular for body centered cubic (bcc) materials such as ferritic steels¹⁷ and tungsten¹⁸, where the brittle-to-ductile transition is known to be controlled by dislocation mobility^{19,20}. Accurate modelling of obstacle hardening in bcc metals is also essential to understand the ductility of oxide dispersion-strengthened steels²¹, which exhibit a large and unexplained strength variability under current manufacture techniques.

Plastic flow in bcc metals is famously controlled by the thermally activated, kink limited motion of $\langle 111 \rangle$ screw dislocations^{22–24}. Due to the large kink pair formation free energy $2F_k(\sigma, T)$, the flow stress of bcc metals is highly temperature dependent even in the absence of obstacles, i.e. $\sigma_F \rightarrow \sigma_F^0(T)$ as $\langle L \rangle \rightarrow \infty$. The plasticity of bcc metals is thus completely incompatible with the Friedel flow stress relationship $\sigma_F \propto 1/\langle L \rangle$, which by construction is athermal and vanishes as $\langle L \rangle \rightarrow \infty$. In studies of bcc plasticity^{8,23–25}, the flow stress σ_F instead emerges as that required to maintain a realistic strain rate.

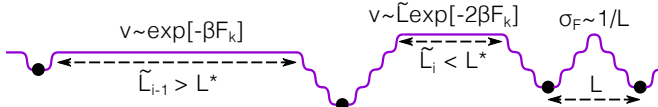


FIG. 2. Three regimes of kink limited motion through obstacles. Left: the key regime identified in this work. When the available segment length $\tilde{L} > L^*$, equation (1), the screw dislocation velocity is length independent and has an activation energy equal to the formation energy of a single kink. Center: when $\tilde{L} < L^*$, the activation energy doubles and the velocity is linearly dependent on the segment length. In both cases, obstacle bypass occurs independently of the obstacle spacing. Right: when obstacles are sufficiently strong or closely spaced, the kink pileups meet before bypass and the dislocation cannot propagate. The critical stress in this regime²⁶ obeys the classical Friedel relationship $\sigma_F \propto 1/L$, where L is the obstacle spacing.

In this paper, we revisit the classic line tension obstacle hardening model, adding a lattice resistance to allow application to modelling bcc plasticity. The inclusion of a kink mechanism induces a qualitative change in dislocation-obstacle interaction, as illustrated in Figure 1B. For realistic applied stresses (well below the Peierls stress¹), dislocations do *not* bow out, as the lattice resistance counteracts the applied stress. Dislocation migration instead occurs through the thermal nucleation and propagation of kink pairs^{23,24}, which form pile-ups at segment pinning points under an applied stress.

Previous studies of the influence of obstacles on kink-limited screw dislocation motion^{8,26–28} have identified a size effect in the limit of densely distributed strong obstacles, where kink pileups forming on either side of pinned segments met, as illustrated in figure 2C. In this case, a segment of length L can support up to $L/(2w_k)$ kink pairs, where w_k is the kink width. The total force exerted by the kink pileups forming on either side of a dislocation segment is $\sigma b h_k L / w_k$, where h_k is the kink height. Equating the pileup force equal to a defined threshold f_{th} , we find $\sigma = w_k f_{\text{th}} / (b h_k L)$, thus recovering the classical Friedel flow stress relationship $\sigma_F \propto 1/\langle L \rangle$. This has been demonstrated in dislocation dynamics simulations²⁶.

Our main result is the identification of a new regime controlled by a well known size effect in the kink nucleation rate^{1,29–31} operative on longer length scales, where the activation energy for kink limited dislocation motion *halves* from $2F_k$ to F_k once the average dislocation segment length L becomes greater than a stress and temperature dependent critical length

$$L^*(\sigma, T) = b \exp [\beta F_k(\sigma, T)]. \quad (1)$$

In this regime, obstacle bypass still occurs once the total force $\sigma b h_k n_k$ exerted by a pile-up of n_k kinks exceeds some defined threshold f_{th} , but the obstacle spacing is sufficiently large that the obstacle bypass occurs before the opposing pileups meet, as shown in the left of figure

2. As a result, in the limit of dilute obstacles the flow behavior is almost independent of the obstacle spacing. For higher obstacle densities the effective dislocation length for kink nucleation is restricted, causing a doubling of the kink nucleation energy and a length dependent dislocation velocity, restricting the rate of plastic flow, as shown in the center of figure 2. Through multiscale simulations and comparison to a wide range of experimental data we show that this provides a powerful model for understanding irradiation induced embrittlement.

Using the Frenkel-Kontorova model²⁹ and kink-limited dislocation-obstacle simulations we evidence a modified Orowan flow law^{23,31,32}

$$\dot{\epsilon} = \begin{cases} \rho b \langle L \rangle \omega_0 \exp [-2\beta F_k(\sigma, T)] & \langle L \rangle \leq L^*(\sigma, T) \\ \rho b^2 \omega_0 \exp [-\beta F_k(\sigma, T)] & \langle L \rangle \geq L^*(\sigma, T), \end{cases} \quad (2)$$

where ρ is the dislocation density. Employing dislocation mobility laws for unirradiated materials parametrized from atomistic simulations^{23,31,33}, we show that under temperatures and applied stresses appropriate for the ductile-brittle transition (DBT), the critical length L^* falls to values of order $10^{-1}\mu\text{m}$, well within the range of typical obstacle spacings $\langle L \rangle$. As illustrated in figure 2, the effective activation energy for dislocation motion thus doubles once the density of obstacles increases and the characteristic obstacle spacing $\langle L \rangle$ falls below L^* , a phenomenon which signifies the onset of embrittlement.

We find compelling agreement with our model through comparison with experimental measurements of the brittle to ductile transition temperature (DBTT) in a wide range of high purity bcc metals³⁴ and neutron-irradiated low activation steels¹⁷. In particular, the *single* kink activation energy flow law is in very good agreement with experimental data on pure materials. This signature is entirely compatible with low temperature bcc plasticity studies²⁵, which find a double kink activation energy as a characteristic parameter in the dislocation mobility law, as in the low temperature regime explored in Ref. 25 the critical length L^* is very large, of order $10^3 - 10^4\mu\text{m}$, and thus the activation energy related BDT transition remains outside the range of parameter space spanned by observations. Applying our model to irradiated materials we find that the DBTT can at most double due to the presence of obstacles, a powerful qualitative relationship which is clearly obeyed in fracture experiments on neutron irradiated low activation steels of widely varying composition.

The paper is structured as follows. In section 1 we explore Frenkel-Kontorova simulations of pinned screw dislocation segments, where the transition in the activation energy for dislocation motion as a function of dislocation segment size is confirmed. In section 2 we review dislocation mobility laws for unirradiated materials, parameterized from atomistic simulations^{23,31,33} and produce quantitative estimates for the stress and temperature dependent critical length $L^*(\sigma, T)$. In section 3 we

condense the observed phenomenology into a simplified dislocation-obstacle interaction model to obtain robust statistical data on the transition in screw dislocation velocity. Finally, in section 4 we compare the predictions of our model to temperature controlled fracture experiments performed on a wide range of unirradiated and irradiated bcc metals.

I. FRENKEL-KONTOROVA SIMULATIONS OF PINNED SCREW DISLOCATIONS

The phenomenology of kink-limited dislocation motion has been extensively studied^{25,33,35} using the stress driven Frenkel-Kontorova model²⁹, which for a line of N nodes with slip plane positions $x_n = (bn, h\xi_n)$, has a potential energy

$$E = \sum_n \frac{\kappa h^2}{2b^2} (\xi_{n+1} - \xi_n)^2 + V \sin^2(\pi \xi_n) - b^2 h \sigma \xi_n, \quad (3)$$

where κ is the line energy of the FK model, V the Peierls barrier and σ the applied stress. Without loss of generality, we choose energy units of V and length units of b . With $h = b$ this system has a Peierls stress $\sigma_p = \pi V / b^3$; setting $\kappa = 200V$ gives a kink energy of $U_k = 40V/\pi$ and a kink width parameter of $10b/\pi$, yeilding the highly mobile kinks appropriate for $\langle 111 \rangle$ screw dislocations in bcc metals³³. For the Frenkel-Kontorova model, the kink free energy is given by $F_k(\sigma, T) \sim U_k(1 - \sigma/\sigma_p)$ for small stresses²². In the kink-limited regime the line velocity v is simply related to the net kink nucleation rate in the direction of the applied stress $\bar{\Gamma} = \Gamma(\sigma) - \Gamma(-\sigma)$ through $v = b\bar{\Gamma}$ ²³. Dynamics are generated using the overdamped Langevin equation with either periodic boundary conditions $\xi_N = \xi_0$ or pinned boundary conditions $\xi_N = \xi_0 = 0$, taking ensemble averages to produce robust statistical data³⁶.

A typical individual simulation configuration is illustrated in figure 3a). For migration distances up to around 25% of the line length, we find the velocity of a pinned line is comparable to that of a periodically repeated dislocation segment of the same length, confirming that the only effect of the pinned boundary conditions is to create two kink pileups, with no effect on the bulk of the line. Figure 3b) demonstrates that for short lines $\bar{\Gamma} \propto L$, but above a certain length threshold $L^*(\sigma, T)$ this becomes length independent. By comparing similar simulations at a range of temperatures, one can extract an activation energy from the slope of an Arrhenius plot ($\beta, \ln \bar{\Gamma}$)³⁷. Combining these simulations, we confirm that for short segments $\Gamma(\sigma) \sim (L/b) \exp[-2\beta F_k(\sigma)]$, whilst for longer segments $\Gamma(\sigma) \sim \exp[-\beta F_k(\sigma)]$, the activation energy thus halving for longer lines (figure 3c)). It is also possible to observe the crossover at a fixed line length simply by varying the temperature and applied stress, as shown in figure 3d). In agreement with literature data^{1,30,31}, we find that the crossover length $L^*(\sigma, T)$ is well predicted by equation (1), $L^*(\sigma, T) = b \exp[\beta F_k(\sigma, T)]$. We

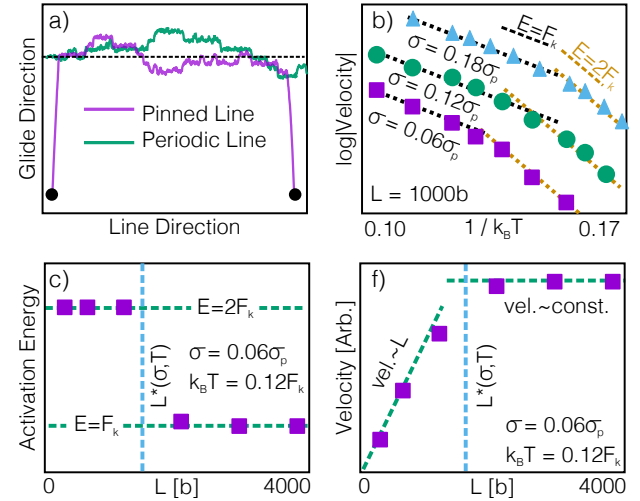


FIG. 3. Frenkel-Kontorova model simulations showing size effects in the kink nucleation rate. a) A pinned and unpinned Frenkel-Kontorova dislocation under applied stress. b) Arrhenius plot of the average velocity. The activation energy halves at high temperature. c) The activation energy halves for segments longer than a critical length $L^*(\sigma, T)$. d) Velocity is proportional to the segment length L below $L^*(\sigma, T)$ and is independent of length above $L^*(\sigma, T)$.

provide a derivation of the crossover length in appendix A.

The dislocation segment size effect on the kink nucleation rate found in our simulations is well known^{1,29–31}, though to the best of our knowledge it has not been previously applied to dislocation-obstacle models. Here, the dependence of the kink nucleation rate $\bar{\Gamma}$ on the segment length L forms the central hardening mechanism in our model, with the crossover length (1) being the critical length scale when comparing to experiment, to a large degree *independent* of the details of dislocation-obstacle interaction.

II. KINK FORMATION FREE ENERGY

Whilst our Frenkel-Kontorova simulations can capture the statistics of the kink nucleation rate as a function of segment length and kink formation energy over a wide parameter range, the intrinsic simplicity of the model clearly cannot reproduce the complex stress and temperature dependence found in fully atomistic simulations^{23,38–40}. In particular, the kink formation free energy and flow stress is known to vanish at both the so-called ‘athermal’ temperature T_{ath} ^{22,41} and a temperature dependent flow stress^{8,22,24,31}. Accommodation of these features is known to be essential to accurately model high temperature screw dislocation motion and thus capture experimental data. Recent calculations of the zero stress double kink formation free energy in tungsten confirms the large contribution of vibrational en-

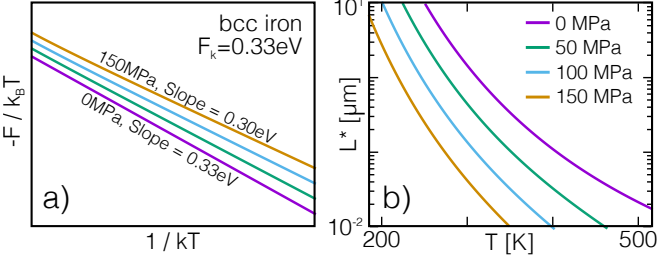


FIG. 4. a) An Arrhenius plot ($-F_k/k_B T, 1/k_B T$) and b) crossover length L^* (1) computed using the kink formation energy (4), with values of $U_k = 0.33\text{eV}$, $\sigma_p = 900\text{MPa}$ and $T_{\text{ath}} = 700\text{K}$ appropriate for a screw dislocation in Fe⁴¹. Applied stress and temperature have dramatic effects on L^* but the effective activation energy changes by less than 10%.

tropic terms which are not predicted in harmonic approximations using static curvatures⁴⁰. Following previous studies, a general approximate form of the kink formation free energy reads^{8,22,24,31,41}

$$F_k(\sigma, T) = U_k \left(1 - \frac{T}{T_{\text{ath}}} - \frac{\sigma/\sigma_p}{1 - T/T_{\text{ath}}} \right). \quad (4)$$

In figure 4a) we show that for realistic applied stresses ($\sigma \lesssim 200\text{MPa}$), an Arrhenius plot of ($-F_k/k_B T, 1/k_B T$) yields a slope that varies by less than 10% for realistic resolved shear stresses (150MPa) present under typical experimental strain rates $\dot{\epsilon} \lesssim 10^{-4}\text{s}^{-1}$, showing that the stress and temperature dependence of (4) predominantly affects the *entropy* (i.e. prefactor) of kink nucleation. The consequences of this entropic boost can be clearly seen, however, when using (4) in our expression (1) for the crossover length L^* , being the characteristic length scale where the effective activation energy for plastic flow halves. As shown in fig 4 for bcc iron, under realistic stresses and temperatures the crossover length can be as low as $10^{-2}\mu\text{m}$, whilst pure materials typically have dislocation mean free paths of the order of μm ⁸. The fact that the crossover length L^* is comparable to typical microstructural length scales is a key factor in the stress, temperature and obstacle density dependence of the brittle-to-ductile transition and is a key conclusion of this paper.

III. DISLOCATION OBSTACLE MODEL

To probe the effect of a random obstacle array on screw dislocation mobility we have used a simplified dislocation-obstacle model which captures the phenomenology of our Frenkel-Kontorova simulations. An initially straight dislocation propagates into an array of obstacles, where it is pinned and split into multiple segments of lengths $\{L_i\}$. As has been noted in previous studies^{26–28}, when a dislocation segment propagates a distance d , the finite kink width w reduces the effective segment length for further kink nucleation to

$\tilde{L}_i = L_i - 2wd/h$, meaning no segment can propagate further than $h\tilde{L}_i/2w$, as illustrated in Figure 2. Using the results above, we assign to each segment a velocity

$$v(\tilde{L}, \sigma, T) = \omega_0 b^2 \left[\frac{1}{L^*(\sigma)} - \frac{1}{L^*(-\sigma)} \right] \frac{\min(L^*, L)}{L^*(\sigma)} \quad (5)$$

where $F_k(\sigma, T)$ is taken from equation (4). Without loss of generality, we set $\sigma > 0$. In the rare event limit the $1/L^*(-\sigma)$ term has a negligible contribution to (5), upon which $\rho bv(\langle L \rangle, \sigma, T)$ is precisely the Orowan flow law (2).

In each realization of our simulations, a simulation cell of width W and height H is populated with a uniformly random array of N obstacles with an initially straight dislocation line lying at the bottom of the cell. The dislocation line is propagated forward a distance d_0 until an obstacle is met, then the global clock time is updated to $t_G = d_0/v(W, \sigma, T)$ and the dislocation line is divided into segments.

A pinned segment of length L will propagate a distance $v(\tilde{L})\Delta t$ in a time Δt , creating an additional $v(\tilde{L})\Delta t/h_k$ kink pairs which pile up at the segment ends. As discussed above, the total force exerted by a kink pile up of height nh_k on an obstacle is given by $n\sigma bh_k$. With a threshold obstacle force f_{th} , the segment will bypass the obstacle once the number of kinks in the pileup exceeds

$$n_{\text{th}} = \frac{f_{\text{th}}}{\sigma bh_k}. \quad (6)$$

In practice, there will be two kink pileups of size n_i^L (n_i^R) on each side of a dislocation segment. When any pileup exceeds n_{th} , the two segments either side of the obstacle are combined, with the remaining kinks propagated to the ends of the new joined segment. The maximum number of kink pairs that the segment can support (as illustrated in figure 2C) is given by $L_i/(2w_k)$. If the corresponding pileup height $L_i h_k/(2w_k)$ is less than n_{th} , the segment will remain pinned until a neighboring segment breaks free. If all the segments are pinned in this manner, the applied stress is not sufficient to induce plastic flow, i.e. we are below the Friedel flow stress, which we ensured did not occur in the simulations used here.

The simulation algorithm is therefore as follows: For each segment i of available nucleation length \tilde{L}_i , the distance \tilde{d}_i to the nearest obstacle is calculated, giving a segment collision time $\tilde{t}_i = \tilde{d}_i/v(\tilde{L}_i)$. The expression for the collision time, accounting for the length dependent mobility, is given in appendix B. The smallest collision time $t_{\min} = \min\{\tilde{t}_i\}$ updates the global clock time $t_G \rightarrow t_G + t_{\min}$; each segment migrates a distance $v(\tilde{L}_i)t_{\min}$, with one segment thus bisected by an obstacle. If the total migration distance past the obstacle on the left or right of a segment is greater than $n_{\text{th}}h_k$, then the neighboring segments are combined and the remaining kinks move to the segment ends. Typical simulation snapshots are shown in the inset of figure 5.

Using this simulation procedure, we can extract the average dislocation velocity and effective activation energy

characterizing plastic flow across a wide range of applied stresses, temperatures and obstacle densities and obstacle strengths. The results of these simulations are shown in figure 5. For low obstacle densities, such that the obstacle spacing is greater than L^* , the dislocation velocity is initially unchanged from the obstacle-free lattice case, with an activation energy being equal to the *single* kink formation energy. However, above a threshold obstacle density (see below), the dislocation velocity drops rapidly and the characteristic activation energy doubles. To recover the same dislocation velocity, the temperature of the system has to effectively double. In the next section we will see that all of this phenomenology is exhibited in fracture experiments on unirradiated and irradiated bcc metals.

To predict the dependence of dislocation motion on the density of obstacles we require an analytic expression for the expected pinned segment length $\langle L \rangle$. Dislocation glide is modeled as planar in a given slip system in our simulations, meaning that a random point obstacle distribution in 3D space with an average density c has an average density cs on the glide plane, where s is the characteristic obstacle size, typically from $4b$ to $10b$. As a dislocation segment will depin from an obstacle once the kink pileup height exceeds $n_{\text{th}}h_k$ **we thus ask for the length $\langle L \rangle$ of a pinned dislocation with n_{th} kinks whose swept area contains a single obstacle.** In appendix C we show this is given by

$$\frac{\langle L \rangle}{w_k} = n_{\text{th}} \left[\frac{\text{erf}(\sqrt{\phi})}{2\sqrt{\phi}} + \frac{2+\phi}{2\phi} e^{-\phi} \right], \quad \phi = csn_{\text{th}}^2 w_k h_k, \quad (7)$$

where $\text{erf}(x) \equiv \int_0^x \exp(-x^2) dx$. This expression takes simple forms for when the kink width w_k ($\sim \sqrt{\kappa/V}$ for a line tension κ and Peierls barrier V ³³) is much larger or smaller than the obstacle spacing. In the limit of a large kink width the swept area is approximately a triangle, yeilding $\langle L \rangle = \sqrt{\pi n_{\text{th}} w_k} / (4\sqrt{c s h_k})$, whilst for a small kink width the swept area is approximately a rectangle, yeilding $\langle L \rangle = 1/(c s n_{\text{th}} h_k)$.

In figure 5, we plot the results of simulations using a fixed obstacle density of $\rho_s \simeq 1/(1500bw_k)$, and thus a fixed $\langle L \rangle$, capturing the effect of variable temperature and stress by varying L^* by around an order of magnitude above and below $\langle L \rangle$. For each value of L^* the average drift velocity was obtained across the same set of 800 independently generated obstacle distributions, uniformly distributed across a discrete grid to avoid very close obstacles (simulating athermal annealing in a real material^{42,43}) with density $\rho_s \simeq 1/(1500bw_k)$. As can be seen, the theoretical prediction (5) using equation (7) for $\langle L \rangle$ gives excellent agreement with our simulations, showing that the length dependent mobility of individual pinned dislocation segments clearly transfers to directly determine the average velocity of dislocation lines moving with kink-limited mobility through a field of obstacles. In particular, for low obstacle densities, where $\langle L \rangle < L^*$, we see that the dislocation velocity is unaffected by the obstacle field, giving a clear single kink activation energy.

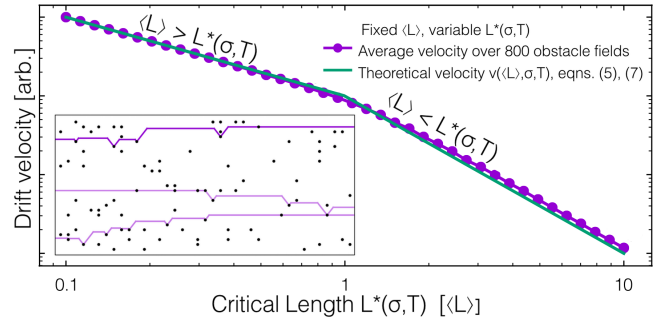


FIG. 5. Predicted and calculated ensemble average velocity with varying critical length at fixed obstacle density, equivalent to varying density at a fixed critical length. Inset: Sample configurations from coarse grained model of screw dislocation-obstacle interactions. Kink pileups are approximated by angled lines rather than steps for computational efficiency.

This behavior is confirmed in the next section, where we compare our model to experimental data.

IV. COMPARISON TO EXPERIMENTS ON PURE AND IRRADIATED BCC METALS

In this section we compare predictions derived from our model to strain and temperature dependent measurements of the brittle-to-ductile transition (BDT) temperature T_{BDT} in a wide range of high purity single crystal bcc metals³⁴ and irradiated low activation ferritic-martensitic steels of great practical importance to the fission and fusion industries¹⁷. In the experiments, small bars of the candidate material are subject to either bending³⁴ or impact¹⁷ tests at a controlled temperature until the sample fractures; in the bending tests the strain rate can also be controlled. The degree of ductility in impact tests is determined by the amount of absorbed energy before fracture. It is well known¹⁹ that in the bending experiments the character of failure mode undergoes a step change as a function of temperature, varying from brittle cleavage at low temperature to semi-brittle fracture to ductile bending over a narrow temperature range termed the brittle-to-ductile transition, with the center of the transition region giving the DBT temperature T_{BDT} .

As embrittlement is known to be controlled by dislocation mobility in bcc metals^{19,20}, the strain rate $\dot{\epsilon}$ and temperature T_{BDT} at which ductile fracture occurs is often interpreted using the Orowan flow law^{23,31,32} $\dot{\epsilon} = pb^2v$. This is equivalent to the statement that ductile fracture occurs at the brittle-to-ductile transition temperature T_{BDT} once dislocation motion can relax the externally applied stresses sufficiently rapidly to avoid failure. Using the expression (2) for the Orowan flow law appropriate for *unirradiated* materials, where the dislocation mean free path is large and $\langle L \rangle > L^*$, our model predicts the simple Arrhenius relation for the *unirradiated* brittle-to-ductile transition

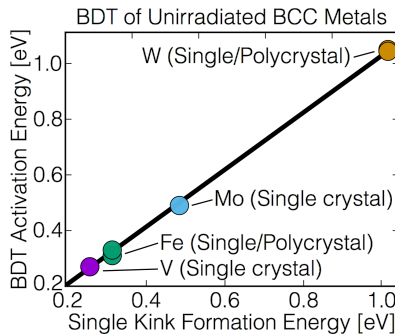


FIG. 6. Plot showing the agreement between characteristic activation energies for the BDT temperature T_{BDT} , derived from an Arrhenius plot of T_{BDT} versus strain rate³⁴, with the *single* kink formation energy predicted by atomistic simulations^{33,35}.

$$\log |\dot{\epsilon}_{\text{unirr}}(T_{\text{BDT}})| = -\frac{U_k}{T_{\text{BDT}}} + S_k + \ln |\rho b^2 \omega_0|. \quad (8)$$

Equation (8) is a main result of this paper, predicting that the characteristic activation energy for ductile fracture in the low obstacle density materials is the *single* kink formation energy $U_k = F_k + TS_k$. As discussed above and illustrated in figure 4, the large kink formation entropy S_k significantly reduces the crossover length L^* to submicron values, i.e. well within the $\langle L \rangle > L^*$ criterion, but due to a fairly weak temperature dependence we find that the observed activation energy should be the single kink formation energy U_k .

We find remarkable agreement with the prediction of equation (8) across a range of high purity unirradiated bcc metals; figure 6 plots the experimentally determined activation energy for ductile fracture against the calculated single kink formation energy using atomistic simulations^{33,35}, showing extremely tight correlation. **The similar fracture behavior for single and polycrystalline tungsten confirms that the dominant fracture mode is transgranular and thus controlled by dislocation mobility.** We emphasize that the clear evidence for a *single* kink formation energy strongly supports a fundamental underlying mechanism of our model, that the characteristic activation energy for kink nucleation energy halves for long screw dislocation segments.

Having verified the predictions of our model on the DBT of unirradiated bcc metals, we now apply it to the interpretation of experiments studying irradiation-induced shifts in the brittle-to-ductile transition temperature T_{BDT} in low activation steels. Due to the greater range of factors involved in the sample preparation, experimental data sets for irradiated materials invariably consider a smaller output parameter space than those for unirradiated materials, complicating detailed interpretation. In particular, changes in the DBTT are typically determined through Charpy impact tests, where the absorbed energy is measured as a function of sample temperature, meaning the imposed strain rate cannot be

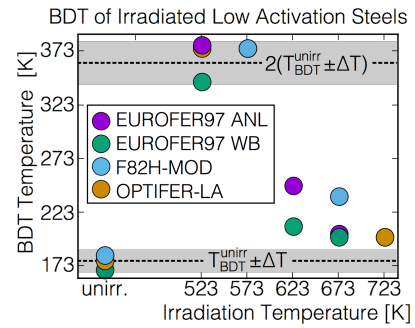


FIG. 7. Observed values of T_{BDT} in various irradiated reduced-activation ferritic/martensitic (RAFM) steels¹⁷, which contain a diverse range of alloying elements. T_{BDT} clearly doubles at high obstacle density (low irradiation temperature), but then returns back to the value characteristic of unirradiated steel as the obstacle density decreases (high irradiation temperature). Importantly, this behaviour is largely independent of the presence of alloying elements.

resolved.

In the experimental data considered here¹⁷, samples of low activation ferritic-martensitic steels were subjected to neutron irradiation to a fixed dose under a fixed irradiation temperature T_{irr} before Charpy impact tests were performed at a range of temperatures. The absorbed energy measured in a Charpy impact test is well known to sharply increase with increasing sample temperature, which is associated with a ductile response⁴⁴; fitting a smooth step function to these data then determines the DBTT. **The fracture was observed to be transgranular, confirming that dislocation mobility, as opposed to grain boundary strength, controlled the mechanical response.** As post-irradiation annealing rates increase with T_{irr} ⁴⁵, positive shifts in the DBTT associated with the accumulation of radiation defect clusters should be suppressed by increasing T_{irr} as the obstacle density decreases.

Figure 7 shows the resultant DBTT data from these experiments¹⁷. A dramatic manifestation of the qualitative behavior described above is clearly observed. The DBTT (expressed in Kelvin units) approximately doubles if the steel samples are exposed to irradiation at relatively low temperature, generating high density of irradiation defect clusters impeding the motion of dislocations, but sharply returns to approximately the unirradiated value over a narrow window of around 50°K in T_{irr} .

Importantly, this behavior is seen across a range of steels with a variety of impurity compositions, indicating that the underlying physics of a sharp doubling of T_{BDT} with irradiation dose if steels are exposed to irradiation at low temperatures is an intrinsic fundamental property of the crystal microstructure rather than the specifics of a particular impurity-defect interaction.

The observed behavior can be simply understood in our model. It is clear that a ductile response to the Charpy impact test requires a similar dislocation velocities for irradiated and unirradiated materials. In the unirradiated case, the temperature required for ductile

flow is $T_{\text{BDT}}^{\text{unirr}} \simeq 173K$. Using the modified Orowan law ² validated in our simulations, the temperature of the brittle to ductile transition in an irradiated material $T_{\text{BDT}}^{\text{irr}}$ can be expressed as

$$T_{\text{BDT}}^{\text{irr}} = \frac{2F_k}{F_k/T_{\text{BDT}}^{\text{unirr}} + \ln |\langle L \rangle/w_k|} \leq 2T_{\text{BDT}}^{\text{unirr}} \quad (9)$$

where the upper bound corresponds to the limit of high obstacle density and small values of $\langle L \rangle$. Using values appropriate for Iron, we find that $T_{\text{BDT}}^{\text{irr}} > 1.8T_{\text{BDT}}^{\text{unirr}}$ for $\langle L \rangle < 100b$, showing that the upper limit is valid for a wide range of obstacle densities. This provides a clear rationalization of the available experimental data, which also shows that the $T_{\text{BDT}}^{\text{irr}}$ is bounded from above by $2T_{\text{BDT}}^{\text{unirr}}$. We also note that the return of the BDT temperature to its value characteristic of unirradiated steels in the limit where samples were exposed to irradiation at high temperature does not imply the absence of obstacles, all that is required for the recovery of the BDT temperature to its original low value is the decrease of the volume density of obstacles, resulting for example from coarsening of microstructure.

V. CONCLUSIONS

In this paper we have introduced a new theory of obstacle hardening for bcc metals, which accounts for the thermally activated flow of $1/2\langle 111 \rangle$ screw dislocations. Via multiscale simulation and theoretical analysis of thermally activated plastic flow through a random obstacle

array, we show that the characteristic activation energy for plastic flow halves when the average obstacle spacing is above a well defined threshold value which depends only weakly on the specifics of dislocation-obstacle interaction and is dominated by the kink formation energy.

Our model predicts that the characteristic activation energy for ductile fracture is the *single* kink formation energy, in excellent agreement with fracture experiments across multiple bcc metals. We also predict that the brittle-to-ductile transition temperature (BDTT) increase following irradiation amounts to at most doubling the BDTT of an unirradiated material, which is also in agreement with fracture experiments on low activation ferritic-martensitic steels. The powerful relationships revealed by our analysis should aid the design of radiation resistant materials; the use of the above model to give quantitative predictions of irradiation-induced shifts in the BDTT require separate estimates of characteristic obstacle distribution, which will be the topic of future work.

VI. ACKNOWLEDGEMENTS

This work has been carried out within the framework of the EUROfusion Consortium and has received funding from the Euratom research and training programme 2014-2018 under Grant Agreements No. 633053 and No. 755039. Also, it has been partially funded by the RCUK Energy Programme (Grant No. EP/P012450/1). The views and opinions expressed herein do not necessarily reflect those of the European Commission. SLD is grateful to I. Lindsey and M.M.E. Coolsen for their critically significant contribution that enabled this research to be carried out.

-
- ¹ J. P. Hirth and J. Lothe, *Theory Of Dislocations* (Malabar, FL Krieger, 1991).
- ² N. Mott, J. Wiley, New York , 173 (1952).
- ³ J. Friedel, *Les Dislocations* (Gauthier-Villars, Paris, 1956).
- ⁴ A. Foreman and M. Makin, Philosophical magazine **14**, 911 (1966).
- ⁵ T. Nogaret and D. Rodney, Physical Review B **74**, 134110 (2006).
- ⁶ S. Patinet and L. Proville, Physical Review B **78**, 104109 (2008).
- ⁷ Y. Dong, T. Nogaret, and W. Curtin, Metallurgical and Materials Transactions A **41**, 1954 (2010).
- ⁸ .
- ⁹ N. M. Ghoniem, S. H. Tong, J. Huang, B. N. Singh, and M. Wen, Journal of Nuclear Materials **307–311**, 843 (2002).
- ¹⁰ D. J. Bacon, Y. Ossetsky, and D. Rodney, in *Dislocations in Solids*, Vol. 15, edited by J. P. Hirth and L. Kubin (Elsevier Science, 2009) pp. 1–90.
- ¹¹ D. Terentyev, S. Hafez Haghigat, and R. Schäublin, Journal of Applied Physics **107**, 061806 (2010).
- ¹² E. Clouet, S. Garruchet, H. Nguyen, M. Perez, and C. S. Becquart, Acta Materialia **56**, 3450 (2008).
- ¹³ L. Dupuy and M. C. Fivel, Acta Materialia **50**, 4873 (2002).
- ¹⁴ S. Brazovskii and T. Nattermann, Advances in Physics **53**, 177 (2004).
- ¹⁵ A. Rosso, P. Le Doussal, and K. J. Wiese, Physical Review B **75**, 220201 (2007).
- ¹⁶ S. J. Zinkle and J. T. Busby, Materials Today **12**, 12 (2009).
- ¹⁷ E. Gaganidze, H.-C. Schneider, B. Dafferner, and J. Aktaa, Journal of Nuclear Materials **355**, 83 (2006).
- ¹⁸ I. Cook, Nature Materials **5**, 77 (2006).
- ¹⁹ P. B. Hirsch, S. G. Roberts, and J. Samuels, Proceedings of the Royal Society of London. A. Mathematical and Physical Sciences **421**, 25 (1989).
- ²⁰ P. Gumbsch, Science **282**, 1293 (1998).
- ²¹ N. Baluc, J. Boutard, S. Dudarev, M. Rieth, J. B. Correia, B. Fournier, J. Henry, F. Legendre, T. Leguey, M. Lewandowska, R. Lindau, E. Marquis, A. Muoz, B. Radiguet, and Z. Oksiuta, Journal of Nuclear Materials **417**, 149 (2011), proceedings of ICFRM-14.

- ²² S. Queyreau, J. Marian, M. R. Gilbert, and B. D. Wirth, *Physical Review B* **84**, 64106 (2011).
- ²³ L. Proville, D. Rodney, and M. C. Marinica, *Nature Materials* (2012).
- ²⁴ D. Cereceda, M. Diehl, F. Roters, D. Raabe, J. M. Perlado, and J. Marian, *International Journal of Plasticity* **78**, 242 (2016).
- ²⁵ D. Brunner, *Materials Transactions, JIM* **41**, 152 (2000).
- ²⁶ G. Monnet, S. Naamane, and B. Devincre, *Acta Materialia* **59**, 451 (2011).
- ²⁷ F. Louchet, L. Kubin, and D. Vesely, *Philosophical Magazine A* **39**, 433 (1979).
- ²⁸ M. Charleux, F. Livet, F. Bley, F. Louchet, and Y. Brechet, *Philosophical Magazine A* **73**, 883 (1996).
- ²⁹ O. M. Braun and Y. S. Kivshar, *The Frenkel-Kontorova Model: Concepts, Methods, and Applications*, Texts and Monographs in Physics (Springer, 2004).
- ³⁰ K. G. Fedorov and A. L. Pankratov, *Physical Review Letters* **103**, 260601 (2009).
- ³¹ G. Po, Y. Cui, D. Rivera, D. Cereceda, T. D. Swinburne, J. Marian, and N. Ghoniem, *Acta Materialia* **119**, 123 (2016).
- ³² E. Orowan, *Proceedings of the Physical Society* **52**, 8 (1940).
- ³³ T. D. Swinburne, S. L. Dudarev, S. P. Fitzgerald, M. R. Gilbert, and A. P. Sutton, *Physical Review B* **87**, 64108 (2013).
- ³⁴ A. A Giannattasio, M. Tanaka, T. D. Joseph, and S. G. Roberts, *Physica Scripta* **T128**, 87 (2007).
- ³⁵ L. Dezerald, L. Proville, L. Ventelon, F. Willaime, and D. Rodney, *Physical Review B* **91**, 094105 (2015).
- ³⁶ T. D. Swinburne, *Physical Review E* **88**, 012135 (2013).
- ³⁷ P. Hänggi, P. Talkner, and M. Borkovec, *Reviews of Modern Physics* **62**, 251 (1990).
- ³⁸ L. Dezerald, L. Ventelon, E. Clouet, C. Denoual, D. Rodney, and F. Willaime, *Physical Review B* **89**, 24104 (2014).
- ³⁹ M. C. Marinica, L. Ventelon, M. R. Gilbert, L. Proville, S. L. Dudarev, J. Marian, G. Bencteux, and F. Willaime, *Journal of Physics: Condensed Matter* **25**, 395502 (2013).
- ⁴⁰ T. D. Swinburne and M. C. Marinica, *Physical Review Letters* **276**, 154 (2018).
- ⁴¹ M. Gilbert, P. Schuck, B. Sadigh, and J. Marian, *Physical Review Letters* **111**, 095502 (2013).
- ⁴² X. Yi, A. E. Sand, D. R. Mason, M. A. Kirk, S. G. Roberts, K. Nordlund, and S. L. Dudarev, *Europhysics Letters* **110**, 36001 (2015).
- ⁴³ T. D. Swinburne, P.-W. Ma, and S. L. Dudarev, *New Journal of Physics* **19**, 073024 (2017).
- ⁴⁴ P. B. Hirsch, J. Samuels, and S. G. Roberts, *Proceedings of the Royal Society of London. A. Mathematical and Physical Sciences* **421**, 1 (1989).
- ⁴⁵ T. D. Swinburne, K. Arakawa, H. Mori, H. Yasuda, M. Isashiki, K. Mimura, M. Uchikoshi, and S. L. Dudarev, *Scientific Reports* **6** (2016).

Appendix A: Derivation of the crossover length

In steady state dislocation glide, where kink nucleation is a rare event, the kink population is in thermal equilibrium and the drift velocity is proportional to the number of kinks¹. As kinks can only be produced in pairs, the kink contribution to the partition function for a line of

length $L = \tilde{N}b$ reads

$$\begin{aligned} Z &= \sum_{r=0}^{\infty} \frac{\tilde{N}! \exp(-2r\beta F_k)}{(\tilde{N}-r)!r!} \\ &= \frac{1}{2} [1 + \exp(-\beta F_k)]^{\tilde{N}} + \frac{1}{2} [1 - \exp(-\beta F_k)]^{\tilde{N}}, \end{aligned} \quad (\text{A1})$$

where the last equality uses the binomial expansion. The expected number of kinks in thermal equilibrium is given by

$$\begin{aligned} \langle n_k \rangle &= -\beta^{-1} \frac{\partial}{\partial F_k} \log Z \\ &= \tilde{N} \frac{e^{-\beta F_k}(1+e^{-\beta F_k})^{\tilde{N}-1} - e^{-\beta F_k}(1-e^{-\beta F_k})^{\tilde{N}-1}}{(1+e^{-\beta F_k})^{\tilde{N}} + (1-e^{-\beta F_k})^{\tilde{N}}}, \end{aligned} \quad (\text{A2})$$

which has two limiting cases of interest- the thermodynamic limit $\tilde{N} \rightarrow \infty$ and the low temperature limit $\beta \rightarrow \infty$. As both appear as powers (A2) these limits will be competing; the thermodynamic limit will be harder to reach at low temperature and *vice versa*. In the thermodynamic limit $\tilde{N} \rightarrow \infty$ we find that

$$\lim_{\tilde{N} \rightarrow \infty} \frac{(1-e^{-\beta F_k})^{\tilde{N}}}{(1+e^{-\beta F_k})^{\tilde{N}}} = 0, \quad (\text{A3})$$

giving an expected kink population of

$$\langle n_k \rangle \rightarrow \frac{\tilde{N}}{\exp(\beta F_k) + 1} \sim \tilde{N} \exp(-\beta F_k), \quad (\text{A4})$$

which is the expected Fermi distribution for *single* kinks. However, in the rare event limit of interest in this work the Boltzmann factor $\exp(-\beta F_k)$ is small ($\sim 10^{-6}$ for room temperature Fe); to *fourth* order in the Boltzmann factor we can make the expansion

$$\langle n_k \rangle \rightarrow \frac{\tilde{N}(\tilde{N}-1)}{2} \exp(-2\beta F_k), \quad (\text{A5})$$

which has the double kink energy. To see where the thermodynamic limit is expected to compete with the low temperature limit, we look for the system size for which $\langle n_k \rangle = 2$ (the smallest possible non-zero population) and solve for \tilde{N} . Approximating $\tilde{N}(\tilde{N}-1) \simeq \tilde{N}^2$ we find a crossover length L^* given by

$$L^* \simeq b \exp(\beta F_k). \quad (\text{A6})$$

Appendix B: Derivation of the segment collision time

Consider a dislocation segment with an available kink nucleation length \tilde{L}_i , as illustrated in figure B.1. Under an applied stress the line will nucleate and accumulate kinks, eventually (in the absence of obstacles or detachment) forming a triangle of height \tilde{L}_i/α , where

$\alpha = w_k/h_k$ is the ratio of kink width to kink height. A finite collision time is therefore only possible if an obstacle lies inside this triangle; we consider such a case, with the obstacle lying a glide distance d away from the line

$$\Delta t(d) = \begin{cases} -\frac{L^*}{2\alpha v_0} \log \left[1 - \frac{2\alpha d}{L^*} \right] & \tilde{L} \leq L^* \\ \frac{\tilde{L} - L^*}{2\alpha v_0} - \frac{L^*}{2\alpha v_0} \log \left[1 - \frac{2\alpha}{L^*} \left(d - \frac{\tilde{L} - L^*}{2\alpha} \right) \right] & L^* < \tilde{L} \leq L^* + 2\alpha d \\ d/v_0 & \tilde{L} \geq L^* + 2\alpha d \end{cases} \quad (\text{B1})$$

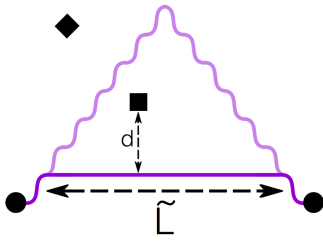


FIG. B.1. Illustration of segment collision time calculation. The maximum propagation state is shown as a transparent line. The diamond obstacle has an infinite collision time as it lies outside the propagation state.

Appendix C: Average segment length in an obstacle field

Consider obstacles uniformly randomly distributed across a space discretized into voxels of volume δV , with an average density ρ . The probability of finding an obstacle in a given voxel is simply $\rho\delta V$; the probability of finding no obstacles in N voxels and then one obstacle in a given further voxel reads

$$\rho\delta V (1 - \rho\delta V)^N. \quad (\text{C1})$$

Let the N voxels fill a closed surface of volume $W = N\delta V$. Taking the continuum limit $\delta V \rightarrow dV$ at constant

segment. Using the rare event limit of the velocity law (5) and defining $v_0 \equiv \omega_0 b \exp(-\beta F_k(\sigma))$ we have three cases for the collision time

W , we find

$$\rho\delta V (1 - \rho\delta V)^N \rightarrow \rho dV \exp(-\rho W), \quad (\text{C2})$$

We now let the volume be a right trapezoid of thickness s , with a fixed angle $\arctan(h_k/w_k)$, maximum height $n_{\text{th}}h_k$ and width L , giving a volume function (easily found geometrically) of

$$W(L) = \begin{cases} sL^2 h_k / w_k & L < n_{\text{th}}w_k \\ sn_{\text{th}}^2 w_k h_k + nn_{\text{th}}h_k(L - n_{\text{th}}w_k) & L \geq n_{\text{th}}w_k \end{cases} \quad (\text{C3})$$

The probability of finding such a volume of width L empty then exactly one obstacle when extending by dL is given by

$$P(\text{obs. } \in [L, L + dL]) = \rho(dW(L)/dL) \exp(-\rho W(L)), \quad (\text{C4})$$

which clearly integrates to one, as eventually at least one obstacle will be found. The average width $\langle L \rangle$ is thus given by

$$\langle L \rangle = \rho \int_0^\infty \rho(dW(L)/dL) \exp(-\rho W(L)) dL, \quad (\text{C5})$$

whose evaluation is in the main text.